Keywords. 1

Using variable-resolution grids to model precipitation from atmospheric rivers around the Greenland ice sheet

Annelise Waling[1], Adam Herrington[2], Katharine Duderstadt[1], Jack Dibb[1], and Elizabeth Burakowski[1]

[1]Institute for the Study of Earth, Oceans, and Space, University of New Hampshire, Durham, NH, USA
[2]National Center for Atmospheric Research, Boulder, Colorado, USA

Correspondence: Annelise Waling (annelisewaling@gmail.com)

Abstract. Atmospheric rivers (ARs) are synoptic-scale features that transport moisture poleward and may cause short duration, high-volume melt events on the Greenland ice sheet (GrIS). In contrast with traditional climate modeling studies that rely on coarse ($1°$ to $2°$) grids, this project investigates the effectiveness of variable-resolution (VR) grids in modeling ARs and their subsequent precipitation using refined grid spacing ($0.25°$ and $0.125°$) around the GrIS and $1°$ grid spacing for the rest of the globe in a coupled land-atmosphere model simulation. VR simulations from the Community Earth System Model (CESM2.2) bridge the gap between the limitations of global and regional climate models while maximizing computational efficiency. ARs from CESM2.2 simulations using three grid types (VR, latitude-longitude, and quasi-uniform) with varying resolutions are compared to outputs from two observation-based reanalysis products, ERA5 and MERRA2, using a study period of 1 January 1979 to 31 December 1998.

The VR grids produce ARs with smaller areal extents and lower area-integrated precipitation over the GrIS compared to latitude-longitude and quasi-uniform grids. We hypothesize that the smaller areal AR extents in VR grids are due to the refined topography resolved in these grids. In contrast, topographic smoothing in coarser resolution latitude-longitude and quasi-uniform grids allows ARs to penetrate further inland on the GrIS. Precipitation rates are similar for the VR, latitude-longitude, and quasi-uniform grids, thus the reduced areal extent in VR grids produce lower area-integrated precipitation. The VR grids most closely match the AR overlap extent and precipitation in ERA5 and MERRA2, suggesting the most realistic behavior among the three configurations.

1 Introduction

Atmospheric rivers (ARs) are large filamentary structures within the atmosphere that contain concentrated amounts of water vapor. ARs originate in the low- to mid-latitudes from synoptic scale systems and subsequently travel poleward. Nearly 90% of total annual polar moisture transport is attributed to ARs (Payne et al., 2020). While there is extensive observation and modeling of ARs over the Pacific and California coast (Huang et al., 2016, 2020; Rhoades et al., 2020b), only recently have studies focused on ARs reaching Greenland (Mattingly et al., 2018, 2020, 2023; Box et al., 2022, 2023; Kirbus et al., 2023). In addition to bringing large amounts of water vapor to the poles, ARs often bring warm temperatures and contribute to snow and ice melt (Bonne et al., 2015; Mattingly et al., 2018, 2020, 2023; Box et al., 2022). Polar regions are already sensitive to feedbacks and warming induced melting, and ARs can exacerbate extreme melting events (Payne et al., 2020). For example, in July 2012 the Greenland ice sheet (GrIS) experienced a short-duration, high-volume melt event in association with an AR that caused substantial mass loss. Bonne et al. (2015) found that during this event, surface mass balance fell three standard deviations below the average value during this time of year and surface melt covered 97% of the GrIS. Before the 2012 event, the most recent instance of melt covering nearly the entire GrIS was 1889 (Neff et al., 2014).

Researchers have predicted and observed an increase in both frequency and intensity of ARs as climate change progresses (Lavers et al., 2015; Hagos et al., 2016; Gershunov et al., 2017; Espinoza et al., 2018; Curry et al., 2019; Huang et al., 2020; Zhang et al., 2021, 2023). This trend suggests that ARs impacting the GrIS surface mass balance, such as the July 2012 event, will increase in frequency. The GrIS experienced multiple major melt events in recent years, including one in August 2021 that was associated with rainfall at Summit Station (Box et al., 2022) and one in September 2022 when at least 23% of the GrIS experienced surface melt (C3S, 2023).

As climate models can help us understand AR dynamics, it is important to determine the model configurations that lead to the most accurate projections. Historically, latitude-longitude grids have been used in climate modeling, but they are highly anisotropic with grid lines converging at the poles (Figure 1a-b). This convergence results in the "polar problem," requiring additional filters to stabilize the numerics, but which also degrades model throughput on massively parallel systems (Herrington et al., 2022). In addition to this numerical instability, the "stretched" shape of latitude-longitude grids leads to high resolution in the zonal direction but lower in the meridional. For improved computational performance, many models use quasi-uniform unstructured grids, e.g., the spectral-element dynamical core (Lauritzen et al., 2018) (Figure 1c-d). These grids use a series of functions to produce grids cells that are roughly equal in size throughout the entire modeling extent, in this case the globe. While these grids eliminate the need for a polar filter and allow for increased computing efficiency, they have coarser spatial resolution in polar regions compared to latitude-longitude grids. Another alternative to traditional latitude-longitude grids common in weather projections (Copernicus, 2019; ECMWF, 2023) is the reduced gaussian grid, which employs quasi-uniformly spaced latitude points and unevenly spaced longitude points to approximate uniform grid size throughout the globe, thus eliminating the need for a polar filter. Variable-resolution (VR) grids, configurations that have increased resolution ($0.25°$ to $0.125°$; Figure 1e and 1f, respectively) in an area of interest, may alleviate some of the negative effects of latitude-longitude schemes, such as the "polar problem", while enabling high spatial resolution in polar regions, though this comes at a higher computation cost compared to coarse uniform grids.

Previous studies have shown the effects of grid configuration choice on AR modeling (Hagos et al., 2015), though questions remain especially regarding high latitude areas. Other studies have found that increasing grid resolution produces more accurate surface mass balance estimates on the GrIS (Noël et al., 2018; Herrington et al., 2022). This work will help the atmospheric community determine when the more computationally expensive (relative to coarse uniform grid spacing) but finer spatial resolution VR grids are most useful, especially given the limited in-situ observations available for quantifying the effects of ARs over Greenland on precipitation and surface mass balance. Models like the Regional Atmospheric Climate Model (RACMO2) (Noël et al., 2018) and other limited area models also provide high spatial resolution, but may be limited by regional boundary conditions and in their ability to simulate climate feedbacks over multi-decadal time scales. In contrast, variable resolution grids provide an intermediate solution between coarse resolution coupled land-atmosphere models, such as CESM2.2, and fine-scale regional climate models that use observation-based forcing data. This paper also details a replicable method for tracking ARs in the Atlantic Arctic region over a multi-decadal simulation, providing insight and guidance into the objective detection of ARs from model data.

This study takes advantage of pre-existing model output from multi-decadal simulations and compares AR characteristics and precipitation produced by six grid configurations using the Community Earth System Model version 2.2 (CESM2.2) (Herrington et al., 2022): two latitude-longitude grids, two quasi-uniform unstructured grids, and two VR grids (Zarzycki and Jablonowski, 2015; Zarzycki et al., 2015). The VR grids used in CESM2.2 employ grid refinement to yield enhanced resolution around Greenland. We hypothesize that the VR grids will simulate ARs more accurately than the coarser resolution grids through better resolution of fine-scale physical processes and topography, as has been seen in other studies investigating moisture intrusions in the Arctic (Ettema et al., 2009; Noël et al., 2018; Bresson et al., 2022). Accurately modeling precipitation from ARs is important because it has been suggested that during early summer nearly 40% of precipitation in Greenland is due to ARs (Lauer et al., 2023). In our study, the model output is compared to the climatology of ARs detected by ERA5 and MERRA2, two observation-based meteorological reanalysis datasets, as in other studies involving simulated ARs (Bresson et al., 2022; Viceto et al., 2022; Zhou et al., 2022; Mattingly et al., 2023). Section 2 describes the model grids, remapping workflow, AR detection method, precipitation counting method, and the validation datasets used in this study. Section 3 contains the main results and analyses performed in this project. Section 4 discusses the implications of these results. Section 5 summarizes main conclusions from our work and provides direction for future research.

2 Methods

2.1 Model simulations

This study uses model output from the CESM2.2 simulations described in Herrington et al. (2022). CESM2.2 contains multiple components, including the Community Atmosphere Model 6 (CAM6) (Craig et al., 2021; Gettelman et al., 2019), the Community Land Model (CLM5) (Lawrence et al., 2019), a sea ice model, the CESM Community Ice Sheet Model (CISM) (Lipscomb et al., 2019), and an ocean model. The simulations were configured with the Atmospheric Model Intercomparison Project protocols, which prescribe monthly sea-surface temperature and sea ice following Hurrell et al. (2008), instead of using the fully coupled ocean and sea-ice models. CISM is not active in the simulations.

CESM2.2 used CAM6 for its physics and atmosphere components. The integrated vapor transport (IVT) fields from the CAM6 simulations were used in AR detection (uIVT, vIVT). CAM6 provided convective precipitation rates and large-scale precipitation rates, which were summed to reach the total atmospheric precipitation, at the lowest atmospheric level. All CAM6 data used in this study was recorded at six-hourly (instantaneous) output intervals. The ERA5 and MERRA2 precipitation variables are also total precipitation, however they are recorded as six-hourly averages, as opposed to instantaneous snapshots.

CESM2.2 used CLM5 for its land component. We used the areal extent of ice based on CLM5 land units to define the GrIS. For Greenland, land unit types include primarily ’Glacier’ and ’Vegetated/Bare Ground’. In our analyses, only ARs touching ’Glacier’ land unit types were considered.

Herrington et al. (2022) ran CESM2.2 simulations using six different grid resolutions (Table 1, Figure 1) from 1 January 1979 to 31 December 1998. These include a two degree latitude-longitude (LL) grid, LL_2° (Figure 1a), a one degree LL grid, LL_1° (Figure 1b), a one degree quasi-uniform unstructured (QU) grid, QU_1.0° (Figure 1c), and another one degree QU grid, but with the physical parameterizations evaluated on a coarser 1.5° grid (Herrington et al. 2019). We refer to this grid as QU_1.5° (Figure 1d), but note the dynamics are still evaluated on the 1° grid. Finally, we use two variable-resolution (VR) grids, VR_0.25° (Figure 1e) and VR_0.125° (Figure 1f), with global spacing of one degree and increased spacing of 0.25 degrees and 0.125 degrees around Greenland, respectively.

Table 1. Description of grid configurations.

grid name	grid type[a]	grid spacing[b] (°)	$\Delta x^{c}_{\text{refine}}$ (°)	ensemble members[d]
LL_2°	LL	2	-	ESMF-QU_1.5°, TR-QU_1.5°, native
LL_1°	LL	1	-	ESMF-LL_2°, ESMF-QU_1.5°, TR-LL_2°, TR-QU_1.5°
QU_1.5°	QU	1[e]	-	ESMF-LL_2°, TR-LL_2°, native
QU_1°	QU	1	-	ESMF-LL_2°, ESMF-QU_1.5°, TR-LL_2°, TR-QU_1.5°
VR_0.25°	VR	1	0.25	ESMF-LL_2°, ESMF-QU_1.5°, TR-LL_2°, TR-QU_1.5°
VR_0.125°	VR	1	0.125	ESMF-LL_2°, ESMF-QU_1.5°, TR-LL_2°, TR-QU_1.5°
ERA5	-	0.25	-	ESMF-LL_2°, ESMF-QU_1.5°, TR-LL_2°, TR-QU_1.5°
MERRA2	-	0.5x0.625	-	ESMF-LL_2°, ESMF-QU_1.5°, TR-LL_2°, TR-QU_1.5°

Table 1. [a]LL = longitude-latitude, QU = quasi-uniform, VR = variable-resolution

[b]Average equatorial grid spacing.

[c]Grid refinement for variable resolution grids.

[d]Remappings performed that were included in the final ensemble. ESMF-LL_2°/TR-LL_2° and ESMF-QU_1.5°/TR-QU_1.5° refer to ESMF and TempestRemap methods which transformed native grids to LL_2° and QU_1.5°, respectively. Note that LL_2° and QU_1.5° grids were not remapped to themselves; their native grid configurations were used.

[e]While QU_1.5° has the same 1° spacing as QU_1°, QU_1.5° has reduced physics resolution, therefore degrading this 1° resolution.

Earth’s topography is a boundary condition for CAM6, and is based on 1 km resolution dataset (Danielson and Gesch, 2011). Software for processing this topography into CAM6 boundary conditions is described in Lauritzen et al. (2015). Figure 2 shows the impact of grid configuration on the resolution of the topography in Greenland. In the coarser grid configurations, LL (Figure 1a-b) and QU (Figure 1c-d), the elevation gradient from the coastal regions to the summit is not well represented. Additionally, high elevations in the center of the GrIS are smoothed in the coarser grids, resulting in a flatter ice sheet. In comparison, the high resolution VR configurations (Figure 1e-f) resolve gradients more similar to the reanalyses.

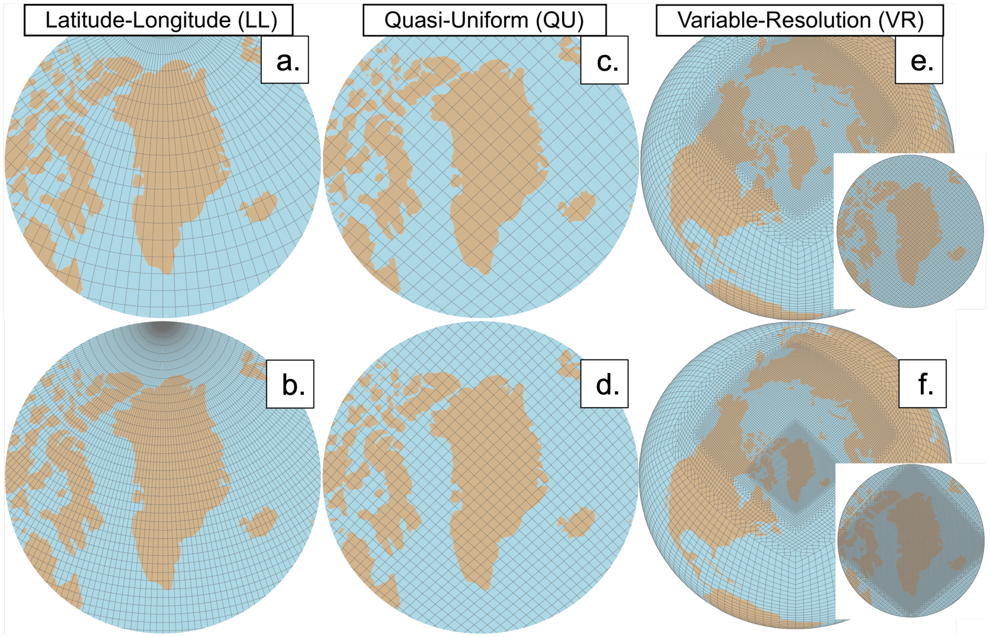

Figure 1. Grids used in this study. a-b) Latitude-longitude (LL) (a- LL_2°, b- LL_1°) grids with higher resolution in polar regions. c-d) Quasi-uniform (QU) (c- QU_1.5°, d- QU_1°) grids with more consistent resolution throughout the globe. e-f) Variable-resolution (VR) (e- VR_0.25°, f- VR_0.125°) with insets emphasizing the higher resolution in the Arctic and Greenland. Lower resolution grids are shown on top row and high resolution on bottom row. Adapted from Herrington et al. (2022)

.

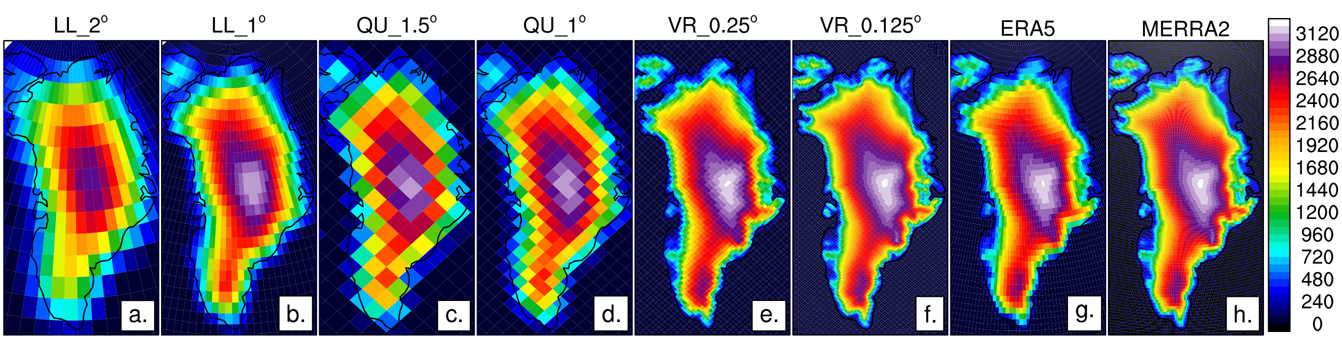

Figure 2. Native topography of each CESM2.2 grid configuration and reanalysis dataset used in this study. A-b show latitude-longitude (LL) (a- LL_2°, b- LL_1°) grids, c-d quasi-uniform (QU) (c- QU_1.5°, d- QU_1°), and e-f variable-resolution (VR) (e- VR_0.25°, f- VR_0.125°), g shows ERA5, and h shows MERRA2.

2.2 Remapping

To control for the sensitivity of the atmospheric feature detection algorithm to grid structure and resolution, we remapped the output from each simulation to the coarsest LL grid (LL_2°) and the coarsest QU grid (QU_1.5°) using two remapping methods, thus resulting in four ensemble members plus the two original coarsest grids (LL_2° and QU_1.5°) for a total of six grid configurations. This was a cautious choice as mapping to higher-resolution grids is inaccurate for first-order methods. The two remapping methods were ESMF (Team et al., 2021) and TempestRemap (Ullrich and Taylor, 2015), both of which use conservative formulations. For each simulation, the algorithm to identify and track ARs described in section 2.3 was run six times, once for each of the four remapped ensemble members and the two coarsest (LL_2° and QU_1.5°) grids.

2.3 Detecting Atmospheric Rivers

Synoptic storms were tracked using TempestExtremes v2.1 atmospheric feature detection software (Ullrich et al., 2021). This algorithm was chosen to detect ARs due to its usage of the Laplacian of the IVT rather than IVT alone. IVT is defined by,

$$IVT = \sqrt{uIVT^2 + vIVT^2} \tag{1}$$

where uIVT and vIVT are pointwise vertically integrated zonal and meridional vapor transport, respectively.

The gradients identified by the Laplacian method can detect ARs more accurately because there will still be a steep gradient between the AR itself and any surrounding moist area, thus better constraining the geometry of the AR (McClenny et al., 2020). Additionally, the use of IVT gradients rather than IVT values themselves generalizes the detection algorithm for use in climates with different amounts of atmospheric water vapor.

While this Laplacian threshold detects AR geometry well, it also allows for non-AR features at high latitudes with similar geometries to be classified as ARs (see Section 3.1). Previous studies have noted the challenges of detecting polar atmospheric rivers due to the east-westward wind patterns that emerge (Rutz et al., 2019). There are many AR tracking algorithms that exhibit different behaviors and are suited to tracking ARs in specific locations (Shields et al., 2018). For example, when detecting Antarctic ARs, trackers that emphasize zonal IVT produce more accurate ARs than other algorithms (Shields et al., 2022). As our study focuses on the impact of resolution on ARs, including a limited number of high latitude regions of moisture transport in the AR analysis does not affect the results.

Two algorithms from the TempestExtremes v2.1 package were used to detect and track ARs: one for detecting ARs (DetectBlobs) and one for stitching ARs together through multiple timesteps (StitchBlobs). The detection algorithm searches the global extent for ARs meeting these parameters: Laplacian of IVT $<$ -30,000 kg m^{-2} s^{-1} rad^{-2}, $>$ 20° latitude, and areal extent $\geq$ 566,666 km^2. The Laplacian IVT threshold was chosen based on Rhoades et al. (2020a), Patricola et al. (2020), and Ullrich et al. (2021). Rhoades et al. (2020a) and Patricola et al. (2020) chose an IVT of -50,000 kg m^{-2} s^{-1} rad^{-2} and Ullrich et al. (2021) used -20,000 kg m^{-2} s^{-1} rad^{-2}. The stricter threshold (-50,000 kg m^{-2} s^{-1} rad^{-2}) resulted in too few land-falling ARs in Greenland, but we still wanted to exclude smaller ARs that may not be of consequence in the GrIS. Thus, our threshold is in the middle of those used by others. The areal extent was chosen conservatively as two-thirds the area of an average AR, which is 850,000 km^2 (A. Rhoades, 2022, personal communication).

The output of the detection algorithm is a binary mask outlining candidate ARs and the stitching algorithm is used to connect the blobs in time, providing each AR its own unique identification number. The stitching algorithm links the ARs detected at each timestep by the detection algorithm, rejecting candidate blobs that are not continuous in time. Using these two algorithms together, we track a single AR across its entire lifespan, from its origin in the mid-latitude regions, poleward transport, and eventual dissipation. We chose to run the stitching algorithm using standard default settings based on optimizations from A. Rhoades (personal communication, 2022). The number of ARs varied based on whether the native grid was remapped to LL_2° or QU_1.5° and the remapping method (Table 2). In addition to this AR tracking, we inventoried the origin points for each detected AR using the maximum IVT for that AR when first detected.

2.4 Compositing variables

To analyze the effects of ARs on precipitation over the GrIS, we first identified all ARs that intersect the GrIS at some point in their lifetimes. We counted all ARs touching the 'Glacier' land units of Greenland in CLM5, determined the overlapping area of these ARs at each timestep, and calculated integrated precipitation from CAM6 output within these areas.

For each ensemble member, the tracker produces a binary mask array $B_n^i(t)$, that contains `1`'s for times t and grid columns n where blob number i is active, and `0`'s elsewhere. Note that there is only one horizontal dimension n, which is the convention for unstructured grids; a second horizontal dimension needs to be added when applying these equations to LL grids, e.g., $B_{x,y}^i(t)$.

We seek to find the time of maximum overlap for each blob, t_c^i, which we define as the time index in which the blob is maximally overlapping with the GrIS. The area of the GrIS covered by blob i for time t is,

$$a^i(t) = \sum_{n=1}^{ncol} \Delta a_n^i(t) \tag{2}$$

where $\Delta a_n^i(t)$ is the overlap area between the GrIS and blob i for each grid cell n,

$$\Delta a_n^i(t) = f_n \Delta A_n B_n^i(t) \tag{3}$$

and ΔA_n is area of each grid cell and f_n is the fraction of each grid cell covered by the GrIS. The time of maximum overlap t_c^i is the time index t for each blob i where $a^i(t)$ is a maximum. Of course, not all blobs descend upon the GrIS throughout their lifetimes. We therefore redefine i to denote the subset of blobs that intersect the GrIS at some point during their lifetime.

To integrate any arbitrary horizontal variable (e.g., precipitation), $x_n(t)$, over the entire GrIS overlap area, coinciding with blob i in the vicinity of the time of maximum overlap $t_c^i + \delta t$,

$$X^i(t_c^i + \delta t) = \sum_{n=1}^{ncol} x_n(t_c^i + \delta t) \Delta a_n^i(t_c^i + \delta t), \tag{4}$$

whereas the area average value of the variable x_n for blob i is,

$$\bar{X}^i(t_c^i+\delta t) = \frac{\sum_{n=1}^{ncol} x_n(t_c^i+\delta t)\Delta a_n^i(t_c^i+\delta t)}{\sum_{n=1}^{ncol} \Delta a_n^i(t_c^i+\delta t)}. \tag{5}$$

The time of maximum overlap t_c^i is used to provide a common reference time for averaging the integrated quantities X^i over all blobs.

We ran this AR characterization process over each of the four ensemble members (ESMF-LL_2°, ESMF-QU_1.5°, TempestRemap-LL_2°, TempestRemap-QU_1.5°) and took the average of each variable over the entire ensemble.

Table 2. Number of ARs intersecting the GrIS.

	ESMF			TempestRemap			
grid name	LL_2°	QU_1.5°	Δ[a]	LL_2°	QU_1.5°	Δ[a]	average[b]
LL_2°	381	339	42	381	281	100	346
LL_1°	431	420	11	510	356	154	429
QU_1.5°	474	485	11	632	485	227	499
QU_1°	483	447	36	596	458	138	496
VR_0.25°	441	404	37	572	405	167	456
VR_0.125°	397	359	38	520	359	161	409
ERA5	426	374	52	425	376	49	400
MERRA2	517	467	50	519	472	47	494

Table 2. [a]Difference (Δ) between LL_2° and QU_1.5° detected ARs intersecting GrIS for each remapping method.
[b]Average takes into account ESMF-LL_2°, ESMF-QU_1.5°, TempestRemap-LL_2°, and TempestRemap-QU_1.5°.

2.5 Validation

Reanalysis data from ERA5 and MERRA2 were used to validate the ensemble generated AR variables. The same remapping and compositing workflow that was applied to CESM2.2 simulations was applied to reanalyses. Meteorological reanalysis datasets combine observational data with a numerical atmosphere model to interpolate spatially and temporally onto a global grid. ERA5 is the fifth reanalysis dataset produced by the European Centre for Medium-Range Weather Forecasts (Hersbach et al., 2020). ERA5 data has horizontal spatial resolution of roughly 27 km and the variables chosen for this study have hourly resolution, though we reprocessed this to six-hourly to match the timesteps in the CESM2.2 model outputs.

The Modern-Era Retrospective Analysis for Research and Applications, version 2 (MERRA2) uses available satellite data, observational data, and the Goddard Earth Observing System (GEOS) model to provide users with a spatially and temporally complete datset (Gelaro et al., 2017). MERRA2 has horizontal resolution of 56 km (latitude) × 69 km (longitude) and three-hourly temporal spacing, which we also reprocessed to six-hourly.

These two reanalysis datasets were chosen as validation due to their frequent application in prior studies (Bresson et al., 2022; Collow et al., 2022; Viceto et al., 2022; Zhou et al., 2022; Mattingly et al., 2023). The CESM2.2 model data and ERA5 share an overlapping study period of 1979-1998. Given that the available MERRA2 data begins in 1980, we chose to include data available from 1980-1999 in order to maintain the same number of years in our study period (1979-1998).

It is important to emphasize that CESM2.2 simulations are free-running, coupled land-atmosphere climate simulations constrained by monthly sea-surface temperature and sea-ice extent, but not by meteorological observations or reanalysis. We therefore present climatological comparisons among model configurations rather than historical observation-based case studies.

3 Results

3.1 Frequency, Seasonality, and Origin Locations of Atmospheric Rivers

Between 7,500 and 10,100 ARs were detected in the Northern Hemisphere across the six model configurations and the two reanalysis products between the years 1979-1998 (1980-1999 for MERRA2) (Figure 3). As MERRA2 includes a different year (1999) than the modeled outputs and ERA5, we ensured that this year experienced a number of ARs that did not vary greatly from 1979-1998 before including it in our analysis. MERRA2 resolved the highest number of ARs at 10,094 and the LL_2° detected the lowest at 7,514. We used the number of ARs intersecting the GrIS (Table 2) and ARs detected globally to calculate the percentage of ARs intersecting the ice sheet. This metric only varied from 4.0% to 5.4%, with ERA5 showing the lowest percentage of ARs reaching GrIS.

The seasonal distribution of ARs reaching Greenland indicates that winter and spring generally have fewer ARs than summer and fall (Figure 4). One or both VR grids produce the same median values as the reanalyses in every season. The QU grids produce the largest number of outliers of the grid configurations. When summed across the seasons, the number of ARs intersecting the Greenland ice sheet on an annual basis ranged from 10-37 per year depending on grid-configuration and specific year. There are large variations from year to year among the grid configurations, as is expected. The reanalyses produce annual variations similar to the spread of modeled simulations, therefore suggesting that the models are producing ARs within or close to the bounds of reanalysis products.

Figure 5 shows the origin locations for each AR that eventually intersects the GrIS during summer months. The origin locations are determined by searching for the grid cell with the maximum IVT inside the AR at the first time that the AR is detected. Note that the location at which an AR forms is sensitive to the Laplacian of the IVT threshold used to identify ARs; a lower threshold means weaker IVT gradients and therefore designates AR origin points at lower latitudes, earlier in the lifespan of an AR. Most ARs intersecting the GrIS during these months form over the central United States from around 30-45° latitude. The next most frequent location for AR formation is over the western Atlantic at similar latitudes. While ARs are defined to originate in low- to mid-latitudes and transport water vapor poleward, the detection algorithm identifies a small number of air masses with IVT characteristics above our detection threshold which originate at high latitudes. If these persist between timesteps, the combination of the detection algorithm and the stitching algorithm designates them as ARs and they are retained

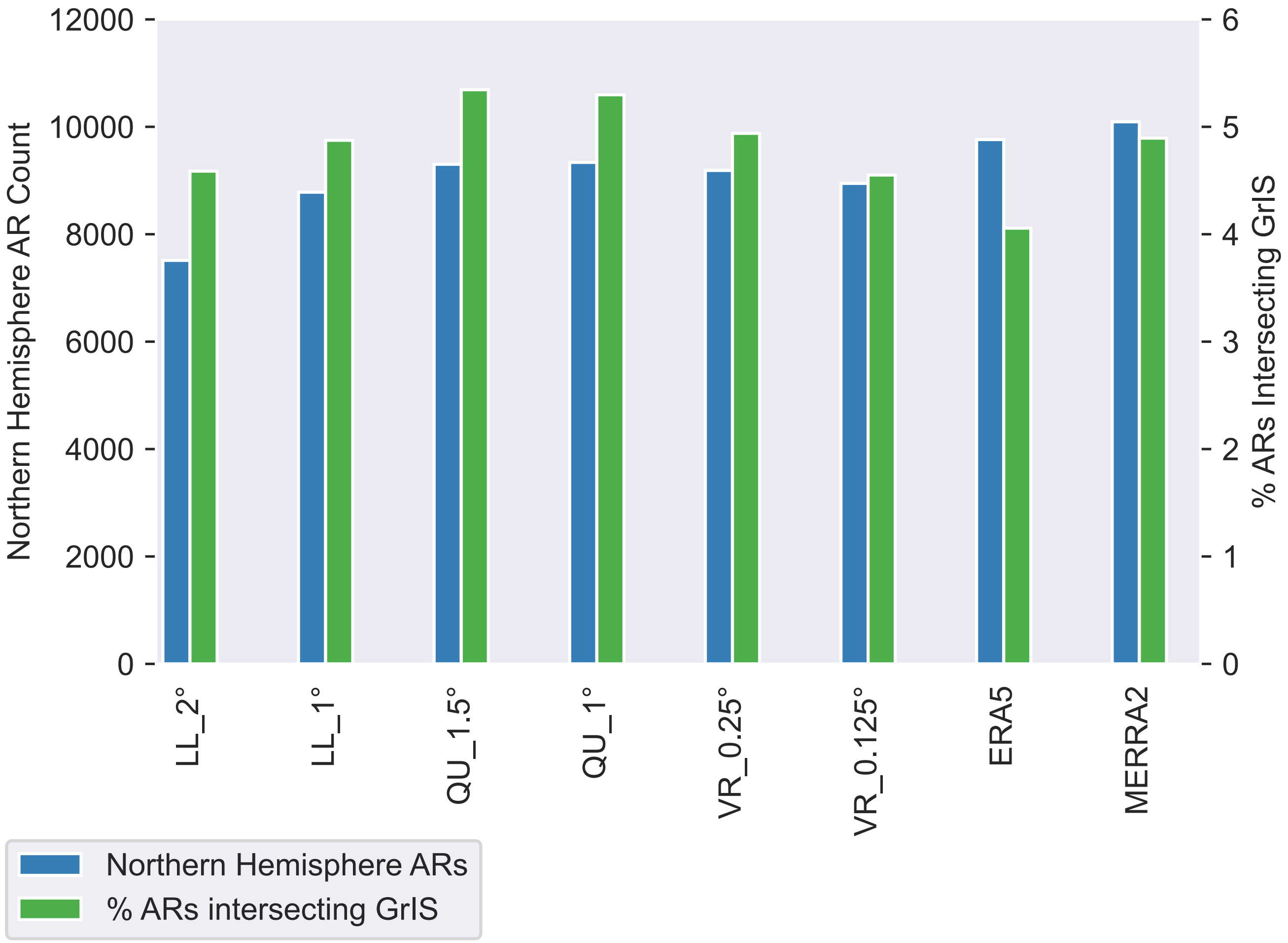

Figure 3. Average number of ARs in the Northern Hemisphere among the ensemble (left axis, blue). Average percentage of ARs intersecting GrIS among ensemble (right axis, green) normalized by total ARs was calculated using data available in Table 2.

in our analysis. Despite these outliers occurring at high latitudes, the majority of identified source regions are consistent with atmospheric rivers developing along mid-latitude storm tracks in relation to the baroclinic instability of extratropical cyclones. The reanalyses have more ARs that originate in the equatorial Atlantic compared to the model simulations.

3.2 Areal Extent of Atmospheric Rivers

The areal extent describes the union of regions on the GrIS that intersect an AR for a particular grid configuration in this study. The VR simulations have the smallest footprints and are most similar to the reanalyses (Table 3). In nearly all cases remapping to the QU_1.5° grid yields smaller footprints than remapping to LL_2°.

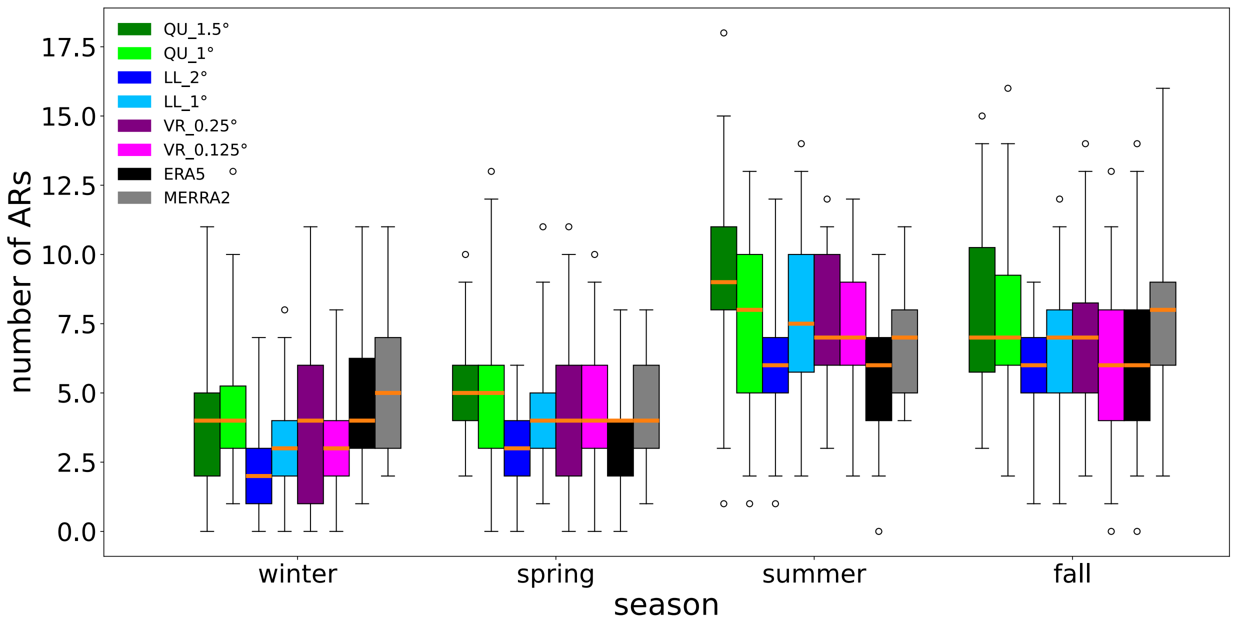

Figure 4. Number of ARs intersecting the Greenland ice sheet by season. Winter was defined as December through February, spring as March through May, summer as June through August, and fall as September through November. Seasonal distributions include 20 years of data (1979-1998) using values from each of the four remapped ensemble members (N=80). Orange line in the center of each box signifies median value and box lower/upper boundaries describe the 25% and 75% quartiles, respectively. The whiskers extend from the box to the 1st and 99th percentiles. Outliers outside these percentiles indicated as open circles.

The variation of footprint size is mainly due to the spatial distribution of ARs across the GrIS (Figure 6). ARs most frequently make landfall with the southwestern and southeastern margins of the GrIS, and the number of ARs per grid cell rapidly declines moving inland for all configurations. ARs modeled with LL and QU grid configurations travel further inland than in the VR grids and reanalyses. It should also be noted that fewer ARs make landfall in the northern portions of the GrIS in ERA5 than any of the other configurations. This lack of northern ARs (Figure 6) explains why ERA5 has the lowest areal extent in Table 3.

3.3 Number and size of atmospheric rivers

Figure 7a shows the number of ARs that eventually intersect the GrIS relative to time of maximum overlap. Five days before the time of maximum overlap roughly 20-25% of the landfalling ARs have formed (Figure A1). This number of ARs increases until the time of maximum overlap, with the largest increase from five days to two days before the time of maximum overlap. This increase up to one day before the time of maximum overlap is likely due to ARs forming at high latitudes (Figure 5). After

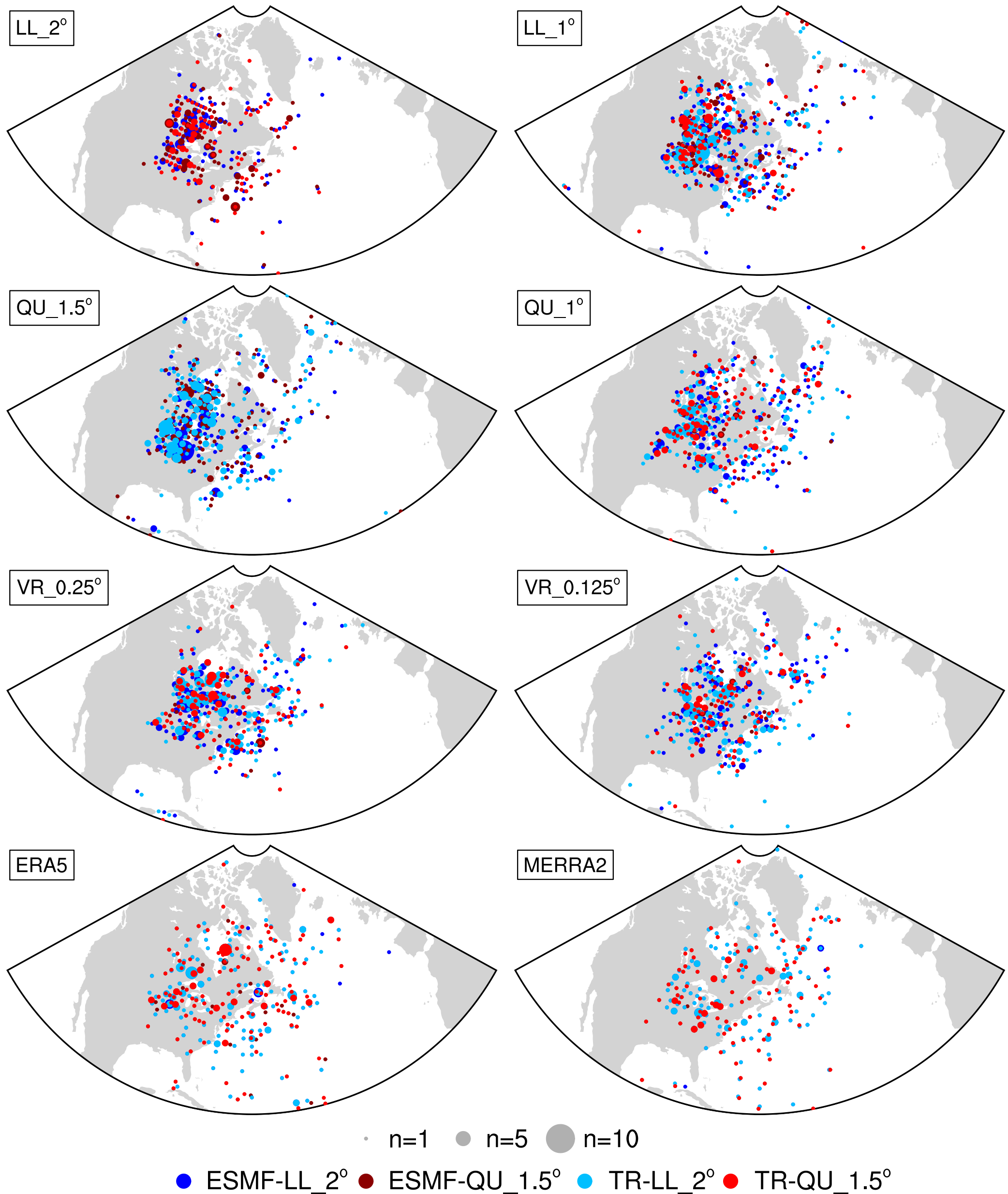

Figure 5. Origin of summer ARs that intersect the GrIS in JJA. The size and color of the dots indicate the number of ARs originating at a given location and the ensemble member represented, respectively.

the time of maximum overlap (i.e., Day 0; Figure 7a), the number of ARs decreases for all grid configurations and reanalyses. The number of ARs one day after the time of maximum overlap is 25-50% lower than the number of ARs during time of

Table 3. Area of ARs intersecting GrIS

grid name	LL_2° areal extent (km^2)^a	QU_1.5° areal extent (km^2)^b	average areal extent (10^5 km^2)^c
LL_2°	1.09x10^6	9.37x10^5	10.1
LL_1°	1.25x10^6	1.17x10^6	12.1
QU_1.5°	1.33x10^6	1.18x10^6	12.5
QU_1°	1.05x10^6	9.82x10^5	10.2
VR_0.25°	8.55x10^5	8.67x10^5	8.6
VR_0.125°	9.80x10^5	8.46x10^5	9.1
ERA5	6.07x10^5	5.11x10^5	5.6
MERRA2	7.11x10^5	6.29x10^5	6.7

Table 3. ^{a}Values are the average of each of the LL_2° ensemble members (ESMF-LL_2°, TempestRemap-LL_2°).
^{b}Values are the average of each of the QU_1.5° ensemble members (ESMF-QU_1.5°, TempestRemap-QU_1.5°)
^{c}Values are the average of each of the four ensemble members (ESMF-LL_2°, ESMF-QU_1.5°, TempestRemap-LL_2°, TempestRemap-QU_1.5°)

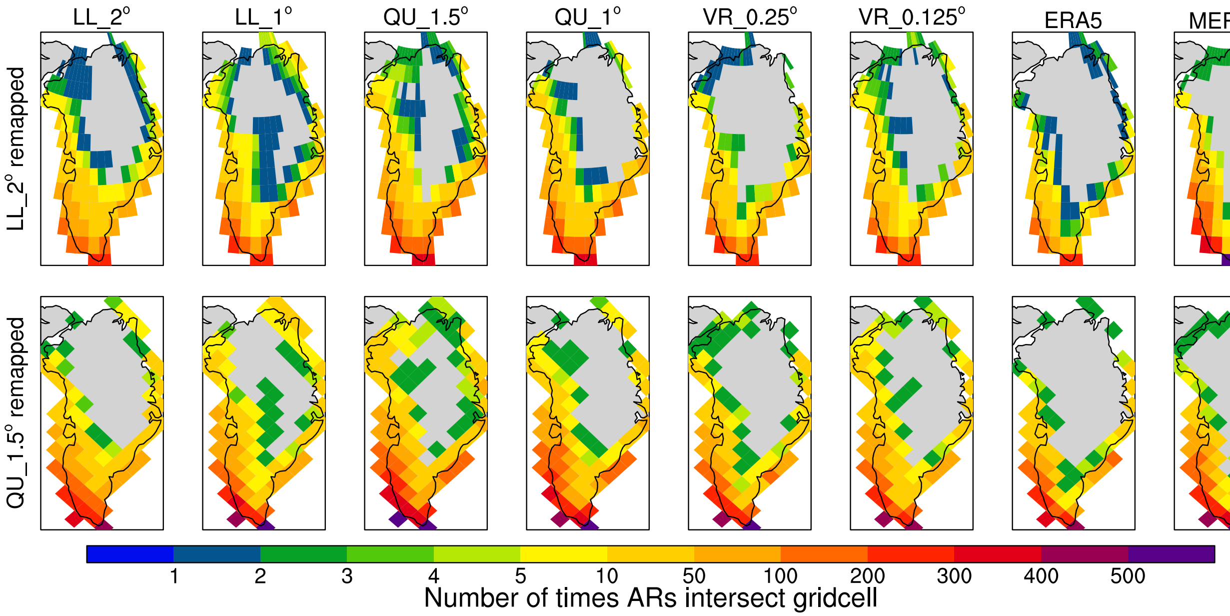

Figure 6. Spatial distribution of ARs over the GrIS using grid configurations remapped to LL_2° and QU_1.5°.

maximum overlap. This means that many ARs rapidly dissipate, suggesting a large moisture transfer from the ARs to the GrIS, although some ARs do continue evolving until around five days past the time of maximum overlap.

Figure 7b describes the number of ARs intersecting the GrIS relative to the time of maximum overlap. The peak storm count at time of maximum overlap in Figure 7b is equal to the ensemble average of storm counts in Table 2. The QU grids produce more ARs than the rest, with the LL, VR, and MERRA2 in the middle, and ERA5 producing the least. Figure 7b also shows that the majority of ARs pass over Greenland in two days, supported by previous research (Mattingly et al., 2020; Box et al., 2023). However, it seems that outside of the +/- one day from maximum overlap, the agreement between outputs degrades. Additionally, outside of that one day window few ARs are actually overlapping the GrIS (< 10 ARs). Thus, needing a larger sample size to calculate meaningful statistics later on, we chose to analyze the ARs over the course of two days, centered by the time of maximum overlap.

Two days before maximum overlap there is a consistent and smooth increase in AR size for all grid configurations and the reanalyses (Figure 7c). This increase continues until one day before maximum overlap where all configurations produce a sharp decrease in AR size due to a rapid reduction of moisture and/or winds. The QU configurations produce the largest ARs for almost the entire study period. After the time of maximum overlap all of the simulations and reanalyses indicate changes in IVT that result in AR area increasing in size again.

The area of an AR overlapping with the GrIS also varies during its lifespan (Figure 7d). In general only a very small portion of each AR overlaps with the GrIS. Average AR areas range from 140-200x1^{10} m^2 but less than 5.0x1^{10} m^2 of any AR is overlapping with the GrIS even during its time of maximum overlap. The LL_2° simulations have the largest overlap area during the time of maximum overlap and onward despite it not having the largest AR area (Figure 7c). Though the QU grids produce the largest ARs (Figure 7c), they do not have the largest overlap area with the GrIS. Reanalyses and the VR grids consistently produce smaller overlap areas.

3.4 Precipitation

When we plot annual mean precipitation rate for all model grids and reanalyses on their native grids (Figure 8), the lower resolution grids tend to produce higher precipitation in the interior of the ice sheet, most notably over the southern dome of the GrIS. While the climatological mean precipitation rate is not exclusively from ARs, it exhibits a similar resolution sensitivity to our AR composite precipitation (Figure 7).

ARs affecting Greenland make landfall on the coasts and travel inland. At this point, much of the moisture deposits as precipitation and the storm dissipates. Figure 9 shows the composite precipitation map of all ARs as they travel over their storm path for one particular grid configuration and remapping scenario. The precipitation rates are largest at the time of maximum overlap with the GrIS, when the storms are at their most inland extent.

We used a two-day window centered on the day of maximum AR overlap (Figure 10a) to composite the area-average cumulative AR precipitation (hereafter, precipitation rate), using equation 5. At the end of the two-day window, there is a difference of around 30 mm between the highest and lowest precipitation rates from the grid configurations and reanalyses. The configuration LL_1° produces the highest rate of precipitation while MERRA2 and LL_2° produces the lowest. ERA5 also produce magnitudes and trends of precipitation similar to the six modeled outputs.

Figure 10b compares the 95th percentile AR precipitation rates. At the end of the study period, the 95th percentile AR precipitation rates differ by about 40 mm, which is similar to the mean precipitation rates. Aside from the scales, the main difference between the mean and extreme rates is the ordering of the model grid configuration. VR_0.125°, VR_0.25°, and

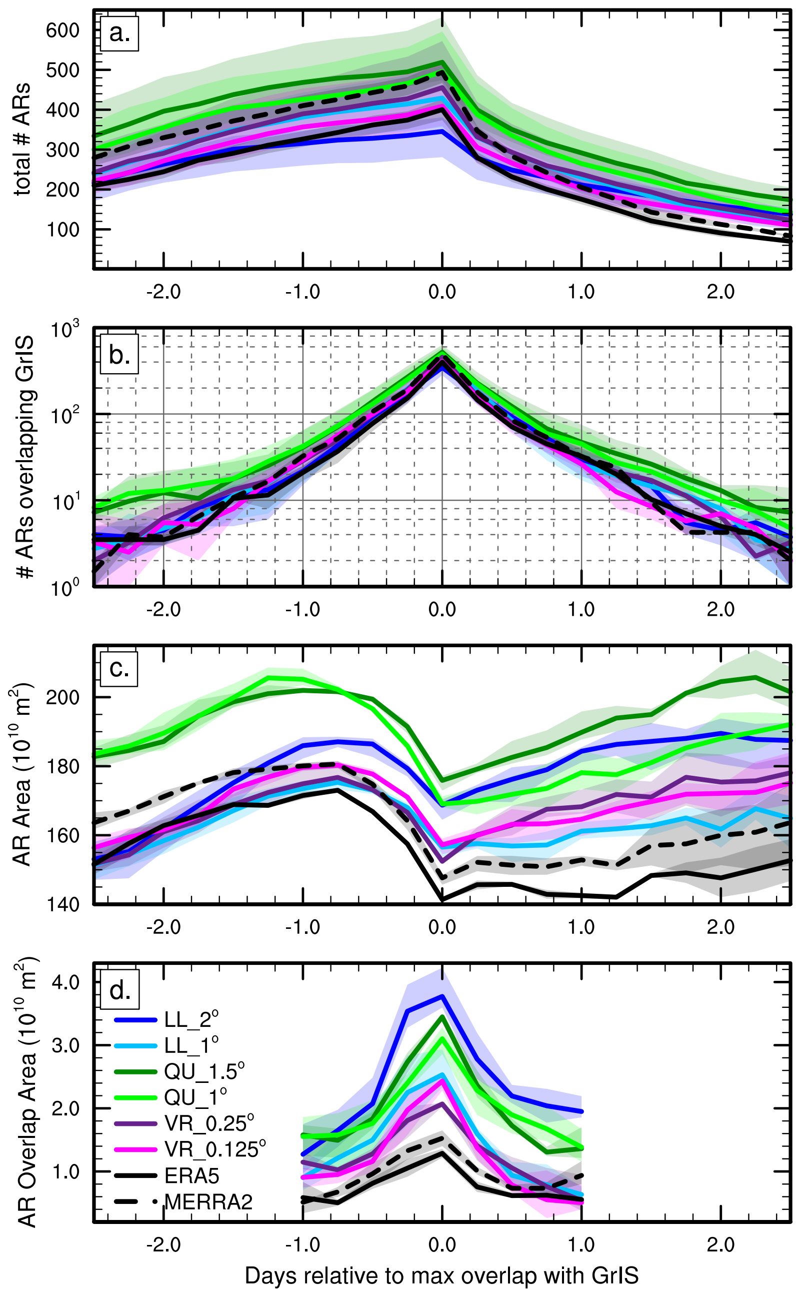

Figure 7. (a) Number of ARs that eventually intersect GrIS as a function of time, normalized as days relative to the time of maximum overlap with GrIS and (b) number of ARs overlapping GrIS. (c) Area (m^2) of ARs that eventually intersect GrIS and (d) area (m^2) of ARs that overlap the GrIS.

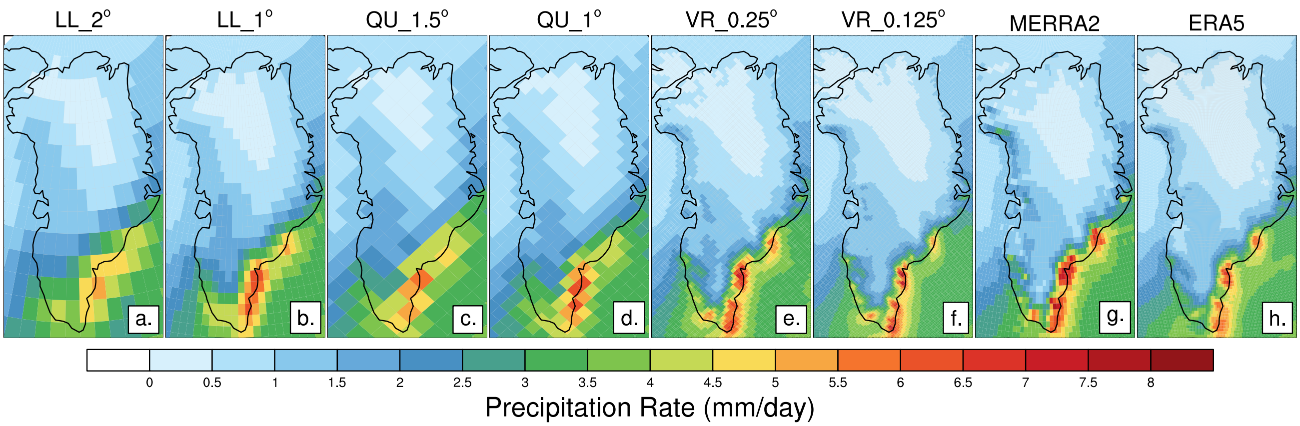

Figure 8. Annual mean precipitation rates (mm/day) for grids and reanalyses used in this study, plotted on their native grids.

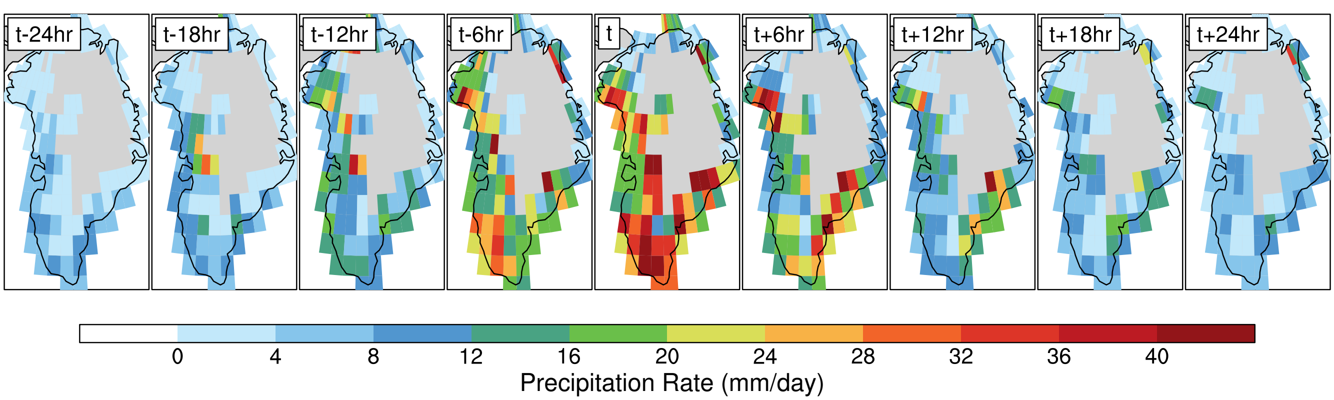

Figure 9. Average precipitation rate (mm/day) over the GrIS during landfalling ARs in an example from the VR_0.125° remapped to LL_2° using ESMF (n = 520 ARs). Time t indicates the time of maximum overlap for the AR over the GrIS.

LL_1° produce higher precipitation rates than MERRA2 and ERA5. This could be related to the model outputs being calculated using six-hourly instantaneous whereas the observation-based data uses six-hourly averages.

Figure 10c compares the average area-integrated cumulative precipitation (hereafter, area-integrated precipitation) (equation 4), showing variation among model outputs and the two reanalyses. Area-integrated precipitation varies from around 0.7 Gt in ERA5 to 2.5 Gt in LL_2°. The two QU grids produce precipitation on the higher end of the spread followed by LL_1°. The two VR grids simulate lower area-integrated precipitation than the other model grids. Both reanalyses produce less precipitation compared to the CESM2.2 model grids, though MERRA2 produces similar precipitation magnitudes to VR_0.125°. There is a difference of about 0.1 Gt between VR_0.125° and MERRA2 and about 0.4 Gt for VR_0.125° and ERA5. The trends in rate of increase of area-integrated precipitation are different than those seen in the precipitation rate (Figure 10a); the highest rate of increase is during the day preceding maximum overlap for all grid configurations except for LL_2°, after which it begins to slow.

Figure 10d compares the 95th percentile area-integrated precipitation. VR_0.125° and VR_0.25° are the most similar model outputs to MERRA2 and ERA5. In particular, VR_0.125° and MERRA2 only differ by around 0.5 Gt in the extreme ARs.

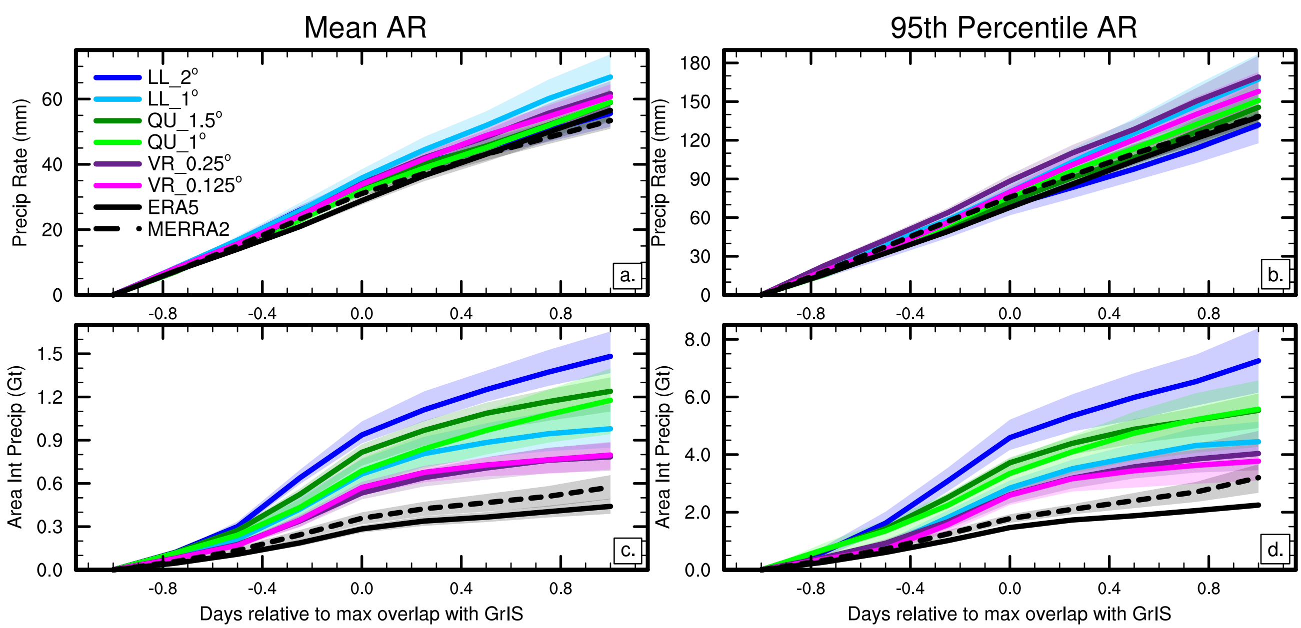

Figure 10. Cumulative precipitation metrics centered around time of maximum AR overlap with GrIS, including (a) mean area-average precipitation rate, (b) 95th percentile precipitation rate, (c) mean area-integrated cumulative precipitation, and (d) 95th percentile cumulative precipitation over the GrIS. Time t indicates the time of maximum overlap for ARs over the GrIS. Precipitation is derived from six-hourly average samples for ERA5 (PRECT), six-hourly average for MERRA2 (PRECTOT), and six-hourly instantaneous for all model simulations (PRECC+PRECL).

A shortcoming of our approach is that we only composite the precipitation inside the tracked feature, however precipitation associated with an AR may include regions outside the tracked feature. Figures 11 and 12 show snapshots from the models and reanalyses, respectively, of the 95th percentile ARs near the time of their maximum overlap with Greenland, and the outline of the detected feature provided in magenta. The detected feature represents the moist core of the AR, which, unlike the larger synoptic system, does not overlap with a large portion of land at any point throughout its lifecycle (Figure 7d). The snapshots indicate the warm front out ahead of the AR core contributes a substantial amount of the storm's precipitation, which have been neglected from our precipitation composites thus far.

Figure 13a quantifies the impact of including regions outside the core of the AR in compositing precipitation due to that AR. It shows the precipitation rates over the two-day window with respect to the radius of the expanded composite area. If a GrIS grid point lies within a radial great circle distance to any point in the detected feature, it is included in the composite. From around 200 km to 500 km, the precipitation rates steadily decrease, as it incorporates regions with smaller magnitude precipitation rates in the composite. From 500 km onward, the precipitation rates decrease at a slower rate, suggesting a transition to the marginal outer regions of the synoptic system which may not be exclusively associated with the storm itself. All model outputs and reanalyses exhibit similar behavior, mainly differing in maximum precipitation rates, with LL_1° having the largest and MERRA2 the smallest.

Figure 13c shows the two-day area-integrated precipitation with respect to radial great circle distance. Similar to the precipitation rates, the integrated precipitation does not change from 0 km to 100 km, as we are analyzing model and reanalysis output mapped to the two coarsest resolution grids. From 200 km to 500 km, the area-integrated precipitation increases due to incorporating a larger area of the GrIS, but which have smaller precipitation rates (Figure 13a). In combining Figures 13a and 13c, we can estimate that most GrIS precipitation which is associated with an AR occurs within around 500 km of the tracked feature. At this 500 km mark, the reanalyses produce between 4.0 Gt and 4.5 Gt of precipitation with both VR outputs well within these bounds. The LL and QU produce between 4.5 to 5.5 Gt and the differences between the VR and LL/QU are even larger at the 1200 km distance. While the coarser grids overestimate GrIS precipitation from ARs, the LL_1.0° is by far the most skillful (Figures 10c, 10d,13c). This is due to the approximate $0.5°$ representation of the GrIS on the LL_1.0° grid (Herrington et al. 2022).

The 95th percentile AR precipitation rate (Figure 13b) and area-integrated precipitation (Figure 13d) exhibit a similar dependence on great circle distance as the mean ARs, although with larger magnitudes. At a radial distance of 500 km, the reanalyses produce roughly 13 Gt precipitation, which is extremely well captured with VR outputs. At 500 km, the LL and QU grids produce between 15-17 Gt precipitation. However, unlike the mean ARs, there is no reduction in precipitation rate from 0 km to 200 km in both reanalysis products. As was suggested for the smaller magnitude precipitation rates in the reanalysis (Figure 10b), this might be due to differences in tracking features and compositing precipitation using six-hourly average reanalysis output instead of six-hourly instantaneous output.

The time-averaging smooths the precipitation and IVT fields over a length-scale determined by the storm's motion and overall evolution, and length of time. This averaging degrades the representation of individual features, which is consistent with only small variations in precipitation in the vicinity of the AR boundary in the reanalyses (Figure 13b). We estimate

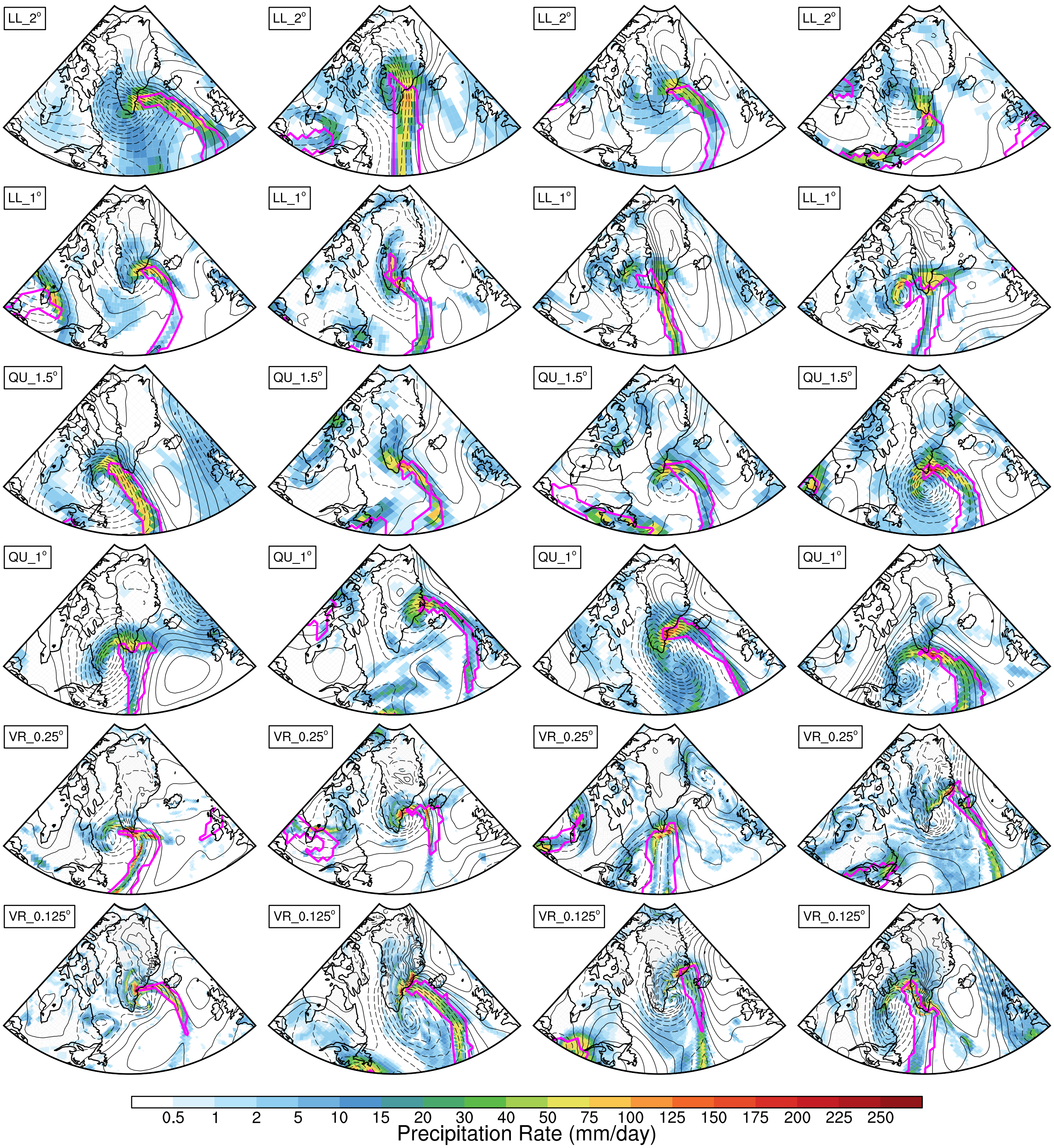

Figure 11. 95th percentile ARs and precipitation rates produced by LL, QU, and VR configurations at four different dates. ARs are outlined in blue. Black contours are sea level pressure anomalies with 5 hPa intervals. Dates are not specified as model runs are free-evolving and do not reflect historical conditions.

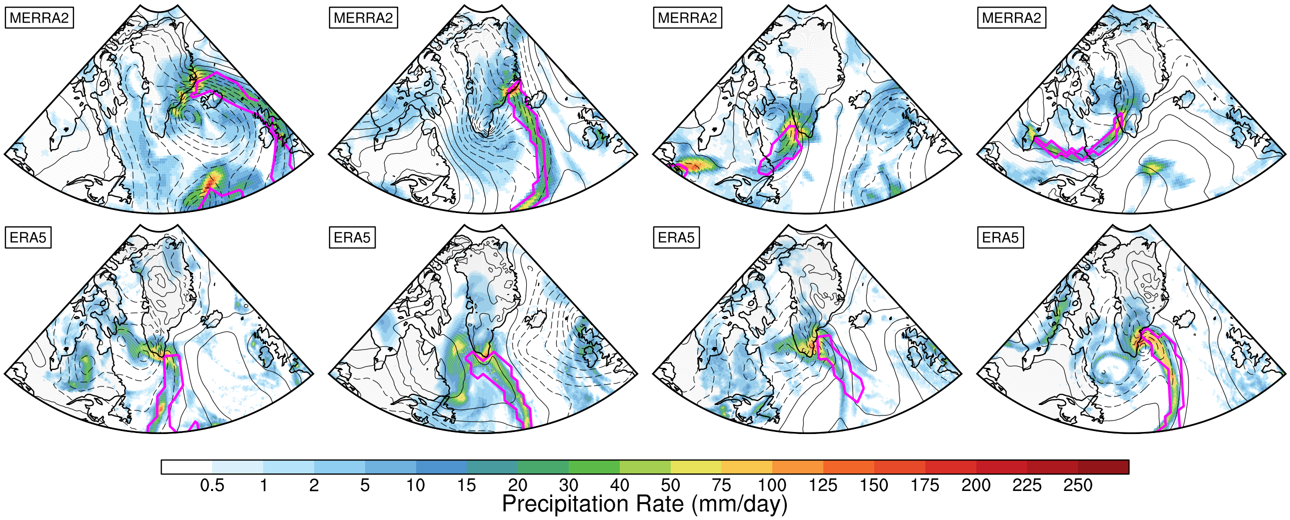

Figure 12. 95th percentile ARs and precipitation rates produced by MERRA2 and ERA5 reanalyses at four different dates. ARs are outlined in blue. Black contours are sea level pressure anomalies with 5 hPa intervals. Dates are not specified for the model AR example figure (Figure 11) and therefore are also not given for this comparison reanalysis figure.

the impact of time-averaging on the VR_0.25° run (Figure 13b). The dotted purple line shows 95th percentile precipitation rate after two-point averaging the six-hourly instantaneous output for tracking the AR and compositing precipitation in the VR_0.25° run. The averaging reduces the magnitude of the precipitation rate and and also reduces the variation across the inner 200 km radial distance (Figure 13b). The reanalysis precipitation rates at the scale of the detected features are smoothed by the time-averaging and cannot serve as a reliable model target for area averages over the detected features (equation 5; Figure 10). That is, we do not conclude that the VR precipitation rates are over-estimated Figure 10, but rather we suggest that the reanalysis precipitation rates and (related) area-integrated precipitation are under-estimated.

The six-hourly time-averaging does not impact the precipitation rates when averaged over larger areas. The VR_0.25° precipitation rates are insensitive to two-point averaging when integrated out to the 500 km radial AR boundary (Figure 13b). We conclude based on Figures 13c-d that the VR grids are able to reproduce the reanalysis and are therefore skillful at simulating precipitation on the GrIS due to ARs.

4 Discussion

We hypothesize that the higher and steeper topography resolved in VR grids and the reanalyses prevent ARs from penetrating as far inland as the ARs do in the LL and QU grids. The finer resolution VR grids and reanalyses produce smaller ARs (Figure 7c), consistent with more precise tracking of atmospheric moisture. However, the large GrIS overlap of ARs in LL_2° (Figure

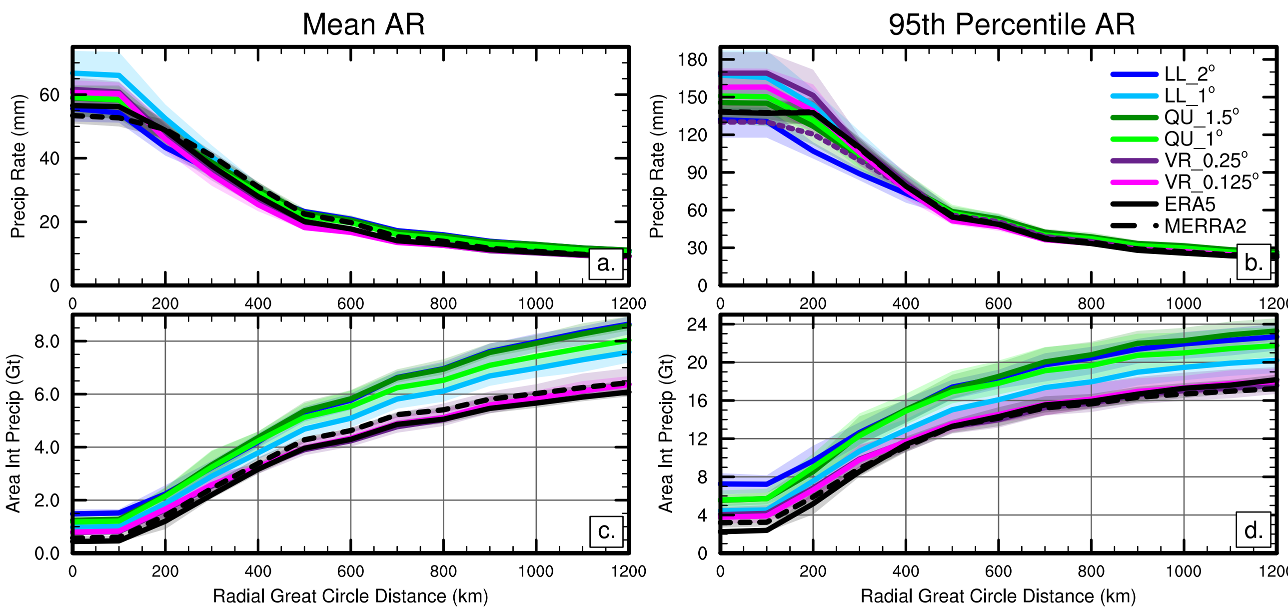

Figure 13. (a) Mean precipitation rates, (b) 95th percentile precipitation rates, (c) mean area-integrated precipitation, and (d) 95th percentile area-integrated precipitation over the GrIS compared to radial great circle distance of GrIS grid points to AR. Radial great circle distance (km) describes the distance of each grid point on the GrIS to an AR. Precipitation is derived from six-hourly instantaneous output in the model runs, whereas the reanalyses use six-hourly averaged precipitation. The dotted purple line in (b) is the VR_0.25° run but using using two-point averaging to estimate the impact of using averaged variables in the reanalyses.

7d) is not related to the size of ARs prior to landfall (Figure 7c), supporting the hypothesis that topographic smoothing explains the variations in AR areal overlap with the GrIS.

Coarser grids require more topographic smoothing to prevent the excitation of inaccurate grid scale modes in the dynamical core (Lauritzen et al., 2015). In the LL and QU grids, topographic smoothing is ubiquitous across the GrIS (Figure 2) and allows for moisture to penetrate further into the interior of the ice sheet, reducing orographic lifting that would otherwise drain ARs of their moisture and cause them to dissipate (Pollard and Groups, 2000; Box et al., 2023). For example, the LL_2° grid has the lowest maximum elevation for the GrIS and the largest AR areal extent. In contrast, the VR grids and reanalysis datasets all have similar topography, capturing high elevations and steep elevational gradients across the GrIS.

The differences in area-integrated precipitation among grid configurations, (Figure 10c-d, Figure 13c-d) reflect the areal extents of ARs over the GrIS (Table 3, Figure 7d). As the precipitation rates are similar across all grids, simulated ARs that cover a larger areal extent of the GrIS deposit more total precipitation. ERA5 produces the lowest area integrated precipitation, followed by MERRA2 and both VR grids, with the LL and QU grids producing the most precipitation. These findings are consistent with the sensitivity of the mean annual precipitation and mass balance across grid resolutions in prior VR CESM studies (Herrington et al., 2022; van Kampenhout et al., 2020).

Previous studies support our hypothesis. Huang et al. (2016) and Rhoades et al. (2020b) have shown that the ability for VR grids to better resolve ARs in regions of complex topography leads to improved simulated climate and snowpack in California. Ikeda et al. (2010) and Ikeda et al. (2021) have found similar results describing the high resolution needed to resolve precipitation and flow around steep topography in the western United States. Regional modeling studies from Ettema et al. (2009) and Franco et al. (2012) also found that reduced topographic smoothing at higher resolution simulations improves storm precipitation in Greenland.

The origin locations and behavior of modeled ARs aligned with observations. We found that many ARs intersecting the GrIS initially form over the mid-latitude central United States (Figure 5), consistent with Neff et al. (2014). Our tracking algorithm also identified a subset of ARs at uncharacteristically high latitudes, suggesting that a more polar-optimized tracking algorithm should be used around Greenland Shields et al. 2023). Alternatively, these high latitude ARs might challenge the typical definition of ARs- does an AR need to form at low- to mid-latitudes? Or are there actually ARs forming at such high latitudes, as Komatsu et al. (2018) and Mattingly et al. (2023) suggest?

ERA5 and MERRA2 differ in geographic distribution of ARs over the GrIS, suggesting the need to consider multiple reanalyses when studying precipitation from ARs in Greenland. While VR grids and MERRA2 produce many ARs making landfall in the northern regions of the GrIS, ERA5 shows very few. Recent studies investigating ARs impacting the northern GrIS support the fact that ARs do occur at such high latitudes in this region (Mattingly et al., 2023).

5 Conclusions

This study uses CESM2.2 simulations from Herrington et al. (2022) to compare six grids in modeling ARs and related precipitation over the GrIS. The 1–2° LL grid configurations provide enhanced resolution over polar regions with some reduction in resolution caused by a polar filter to prevent numerical instability. Two QU grids maintain roughly 1–1.5° uniform resolution throughout the globe. To study the impact of resolution on ARs around the GrIS, we compare simulations using these four coarser grids to two VR grids using the spectral-element dycore, VR_$0.25°$ and VR_$0.125°$.

We developed a method that maps all output to the two coarsest model grids using two different remapping methods to account for uncertainty of comparing AR statistics in model simulations and reanalysis products across vastly different grids. We use the overlap area of an AR and the GrIS to determine how AR characteristics and precipitation varies based on grid configuration. This method attributes precipitation from regions of the GrIS that an AR is directly overlapping at a point in time and sums the precipitation in each of these regions by grid configuration. This allows for a robust comparison of precipitation across grids with realistic uncertainty. We also employ a method expanding on the area directly below an AR to better estimate precipitation derived from these events. This method ideally can also be applied to other variables relevant to ARs and the GrIS, including snowmelt and radiative fluxes (Mattingly et al., 2020; Kirbus et al., 2023)

We find that the topographic resolution of the grid likely constrains AR penetration into the GrIS. In coarser resolution grids, there is greater topographic smoothing of the GrIS and ARs can travel further inland. As precipitation rates do not vary greatly across grid configurations, the overlap extent of ARs largely determines the simulated precipitation falling onto the GrIS. Additionally, we see consistent patterns characterizing AR behavior and lifespan around the GrIS. In the CESM2.2 simulations and reanalyses, most ARs only intersect the GrIS for around one to two days. ARs increase in intensity prior to landfall, and immediately before the time of maximum overlap ARs experience a "draining period" and decrease in size, likely due to orographic uplift that drains the ARs of their moisture. The role of smoothed topography could be further explored by running the model with the VR grid but using the same lower resolution topography as the coarser grids.

Finally, we find that the VR grids produce AR areal extents, area-integrated precipitation, and AR sizes that are most similar to the reanalysis datasets ERA5 and MERRA2. All CESM2.2 simulations produce higher values for all three AR metrics than the reanalyses. Although VR grids deviate some from the reanalyses, VR grids outperform the LL and QU grids used in our study and have resolutions approaching regional climate models but at lower computational costs. We therefore recommend modeling studies of ARs around Greenland consider using CESM2.2 VR grid configurations as an alternative to uniform grids.

Code and data availability. The code and data presented in main part of this manuscript are available at https://github.com/adamrher/greenland-storms.

Author contributions. AW wrote manuscript and assisted with code preparation and ran analysis code. AH prepared methodology and developed data processing code. EB secured project funding and resources for initial project conceptualization. All co-authors provided edits and revisions to the manuscript, data analysis, and synthesis.

Competing interests. The authors declare that they have no conflict of interest.

Acknowledgements. Funding support for this work was provided in part by the National Science Foundation Established Program to Stimulate Competitive Research (EPSCoR NSF-OIA #1832959), the Navigating the New Arctic NSF Research Traineeship (NNA-NRT; NSF-DGE #2125868) Program, the University of New Hampshire (UNH) Institute for the Study of Earth, Oceans, and Space, the UNH Department of Earth Sciences Teaching Assistantship, the UNH Graduate School Summer Teaching Assistant Fellowship, and the NASA Space Grant Fellowship (NH) (NASA 80NSSC20M0051).

This material is based upon work supported by the National Center for Atmospheric Research (NCAR), which is a major facility sponsored by the NSF under Cooperative Agreement #1852977. Computing and data storage resources, including the Cheyenne supercomputer (Computational and Information Systems Laboratory, 2017), were provided by the Computational and Information Systems Laboratory (CISL) at NCAR.

Appendix A: Ten day atmospheric river size and Greenland ice sheet intersection simulation

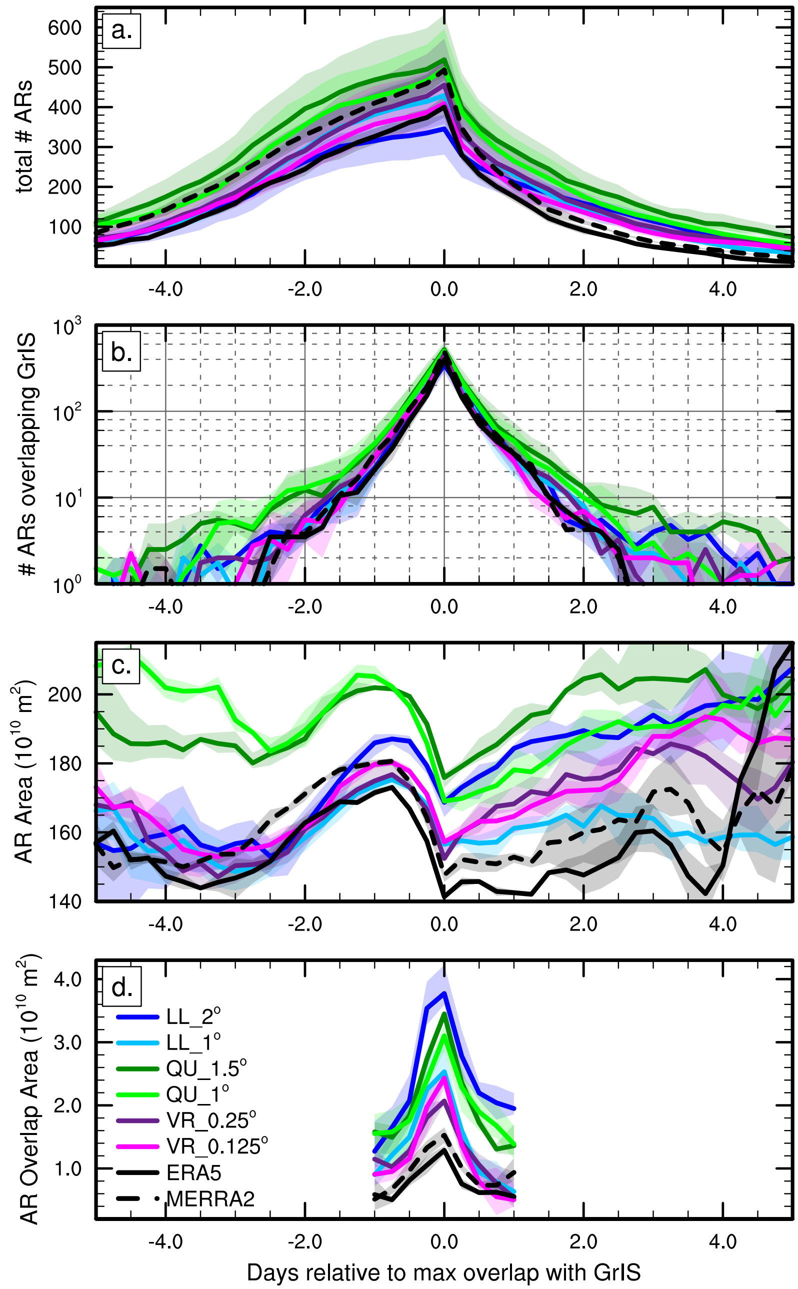

Figure A1. (a) Number of ARs that eventually intersect GrIS as a function of time, normalized as days relative to the time of maximum overlap with GrIS and (b) number of ARs overlapping GrIS. (c) Area (m^2) of ARs that eventually intersect GrIS and (d) area (m^2) of ARs that overlap the GrIS, showing that only a small portion of each AR overlaps the GrIS. As data is noisy at the beginning and end of the ten period, main text only includes +/- 2.5 days.

References

Bonne, J.-L., Steen-Larsen, H. C., Risi, C., Werner, M., Sodemann, H., Lacour, J.-L., Fettweis, X., Cesana, G., Delmotte, M., Cattani, O., and et al.: The summer 2012 Greenland Heat Wave: In situ and remote sensing observations of water vapor isotopic composition during an Atmospheric River Event, Journal of Geophysical Research: Atmospheres, 120, 2970–2989, https://doi.org/10.1002/2014jd022602, 2015.

Box, J. E., Wehrlé, A., van As, D., Fausto, R. S., Kjeldsen, K. K., Dachauer, A., Ahlstrøm, A. P., and Picard, G.: Greenland ice sheet rainfall, heat and albedo feedback impacts from the mid-august 2021 Atmospheric River, Geophysical Research Letters, 49, https://doi.org/10.1029/2021gl097356, 2022.

Box, J. E., Nielsen, K. P., Yang, X., Niwano, M., Wehrlé, A., van As, D., Fettweis, X., Køltzow, M. A., Palmason, B., Fausto, R. S., and et al.: Greenland ice sheet rainfall climatology, extremes and Atmospheric River Rapids, Meteorological Applications, 30, https://doi.org/10.1002/met.2134, 2023.

Bresson, H., Rinke, A., Mech, M., Reinert, D., Schemann, V., Ebell, K., Maturilli, M., Viceto, C., Gorodetskaya, I., and Crewell, S.: Case study of a moisture intrusion over the Arctic with the icosahedral non-hydrostatic (ICON) model: Resolution dependence of its representation, Atmospheric Chemistry and Physics, 22, 173–196, https://doi.org/10.5194/acp-22-173-2022, 2022.

C3S, C. C. C. S.: European State of the Climate 2022, Full report, climate.copernicus.eu/ESOTC/2022, 2023.

Collow, A. B., Shields, C. A., Guan, B., Kim, S., Lora, J. M., McClenny, E. E., Nardi, K., Payne, A., Reid, K., Shearer, E. J., and et al.: An overview of ARTMIP's tier 2 reanalysis intercomparison: Uncertainty in the detection of atmospheric rivers and their associated precipitation, Journal of Geophysical Research: Atmospheres, 127, https://doi.org/10.1029/2021jd036155, 2022.

Computational and Information Systems Laboratory: Cheyenne: HPE/SGI ICE XA System (Climate Simulation Laboratory), Boulder, CO: National Center for Atmospheric Research, https://doi.org/10.5065/D6RX99HX, 2017.

Copernicus, C.: ERA5 monthly averaged data on pressure levels from 1979 to present, URL: https://cds. climate. copernicus. eu, https://doi.org/10.24381/cds.6860a573, 2019.

Craig, C., Bacmeister, J., Callaghan, P., Eaton, B., Gettelman, A., Goldhaber, S. N., Hannay, C., Herrington, A., Lauritzen, P. H., McInerney, J., Medeiros, B., Mills, M. J., Neale, R., Tilmes, S., Truesdale, J., Vertenstein, M., and Vitt, F. M.: CAM6.3 User's Guide, Tech. rep., NCAR/TN-571+EDD, https://doi.org/10.5065/Z953-ZC95, 2021.

Curry, C. L., Islam, S. U., Zwiers, F. W., and Déry, S. J.: Atmospheric rivers increase future flood risk in western Canada's largest Pacific River, Geophysical Research Letters, 46, 1651–1661, https://doi.org/10.1029/2018gl080720, 2019.

Danielson, J. and Gesch, D.: Global Multi-resolution Terrain Elevation Data 2010 (GMTED2010), Open-file report 2011-1073, U.S. Geological Survey, http://pubs.usgs.gov/of/2011/1073/pdf/of2011-1073.pdf, 2011.

ECMWF: IFS Documentation CY48R1 - Part III: Dynamics and Numerical Procedures, 3, ECMWF, https://doi.org/10.21957/26f0ad3473, 2023.

Espinoza, V., Waliser, D. E., Guan, B., Lavers, D. A., and Ralph, F. M.: Global analysis of climate change projection effects on Atmospheric Rivers, Geophysical Research Letters, 45, 4299–4308, https://doi.org/10.1029/2017gl076968, 2018.

Ettema, J., van den Broeke, M. R., van Meijgaard, E., van de Berg, W. J., Bamber, J. L., Box, J. E., and Bales, R. C.: Higher surface mass balance of the Greenland ice sheet revealed by high-resolution climate modeling, Geophysical Research Letters, 36, https://doi.org/10.1029/2009GL038110, 2009.

Franco, B., Fettweis, X., Lang, C., , and Erpicum, M.: Impact of spatial resolution on the modelling of the Greenland ice sheet surface mass balance between 1990–2010, using the regional climate model MAR, The Cryosphere, 6, 695–711, https://doi.org/10.5194/tc-6-695-2012, 2012.

Gelaro, R., McCarty, W., Suárez, M. J., Todling, R., Molod, A., Takacs, L., Randles, C. A., Darmenov, A., Bosilovich, M. G., Reichle, R., and et al.: The modern-era retrospective analysis for research and applications, version 2 (merra-2), Journal of Climate, 30, 5419–5454, https://doi.org/10.1175/jcli-d-16-0758.1, 2017.

Gershunov, A., Shulgina, T., Ralph, F. M., Lavers, D. A., and Rutz, J. J.: Assessing the climate-scale variability of Atmospheric Rivers affecting western North America, Geophysical Research Letters, 44, 7900–7908, https://doi.org/10.1002/2017gl074175, 2017.

Gettelman, A., Hannay, C., Bacmeister, J. T., Neale, R. B., Pendergrass, A., Danabasoglu, G., Lamarque, J.-F., Fasullo, J., Bailey, D., Lawrence, D., et al.: High climate sensitivity in the Community Earth System Model version 2 (CESM2), Geophysical Research Letters, 46, 8329–8337, 2019.

Hagos, S., Leung, L. R., Yang, Q., Zhao, C., and Lu, H.: Resolution and Dynamical Core Dependence of Atmospheric River Frequency in Global Model Simulations, Journal of Climate, 28, 2764–2776, https://doi.org/10.1175/JCLI-D-14-00567.1, 2015.

Hagos, S. M., Leung, L. R., Yoon, J., Lu, J., and Gao, Y.: A projection of changes in landfalling atmospheric river frequency and extreme precipitation over western North America from the large ensemble CESM simulations, Geophysical Research Letters, 43, 1357–1363, https://doi.org/10.1002/2015gl067392, 2016.

Herrington, A. R., Lauritzen, P. H., Lofverstrom, M., Lipscomb, W. H., Gettelman, A., and Taylor, M. A.: Impact of grids and dynamical cores in CESM2.2 on the surface mass balance of the Greenland Ice Sheet, Journal of Advances in Modeling Earth Systems, 14, https://doi.org/10.1029/2022ms003192, 2022.

Hersbach, H., Bell, B., Berrisford, P., Hirahara, S., Horányi, A., Muñoz-Sabater, J., Nicolas, J., Peubey, C., Radu, R., Schepers, D., and et al.: The ERA5 global reanalysis, Quarterly Journal of the Royal Meteorological Society, 146, 1999–2049, https://doi.org/10.1002/qj.3803, 2020.

Huang, X., Rhoades, A. M., Ullrich, P. A., and Zarzycki, C. M.: An evaluation of the variable-resolution CESM for modeling California's climate, Journal of Advances in Modeling Earth Systems, 8, 345–369, https://doi.org/10.1002/2015MS000559, 2016.

Huang, X., Swain, D. L., and Hall, A. D.: Future precipitation increase from very high resolution ensemble downscaling of Extreme Atmospheric River Storms in California, Science Advances, 6, https://doi.org/10.1126/sciadv.aba1323, 2020.

Hurrell, J. W., Hack, J. J., Shea, D., Caron, J. M., and Rosinski, J.: A new sea surface temperature and sea ice boundary dataset for the Community Atmosphere Model, Journal of Climate, 21, 5145–5153, 2008.

Ikeda, K., Rasmussen, R., Liu, C., Gochis, D., Yates, D., Chen, F., Tewari, M., Barlage, M., Dudhia, J., Miller, K., and Arsenault, K.: Simulation of seasonal snowfall over Colorado, Atmospheric Research, 97, 462–477, https://doi.org/10.1016/j.atmosres.2010.04.010, 2010.

Ikeda, K., Rasmussen, R., Liu, C., Newman, A., Chen, F., Barlage, M., Gutmann, E., Dudhia, J., Dai, A., L., C., and Musselman, K.: Snowfall and snowpack in the Western US as captured by convection-permitting climate simulations: current climate and pseudo global warming future climate, Climate Dynamics, 57, 2191–2215, https://doi.org/10.1007/s00382-021-05805-w, 2021.

Kirbus, B., Tiedeck, S., Camplani, A., Chylik, J., Crewell, S., Dahlke, S., Ebell, K., Gorodetskaya, I., Griesche, H., Handorf, D., and et al.: Surface impacts and associated mechanisms of a moisture intrusion into the Arctic observed in mid-April 2020 during mosaic, Frontiers in Earth Science, 11, https://doi.org/10.3389/feart.2023.1147848, 2023.

Komatsu, K. K., Alexeev, V. A., Repina, I. A., and Tachibana, Y.: Poleward upgliding siberian atmospheric rivers over sea ice heat up Arctic Upper Air, Scientific Reports, 8, https://doi.org/10.1038/s41598-018-21159-6, 2018.

Lauritzen, P. H., Bacmeister, J. T., Callaghan, P. F., and Taylor, M. A.: NCAR global model topography generation software for unstructured grids, Geoscientific Model Development Discussions, 8, 4623–4651, https://doi.org/10.5194/gmdd-8-4623-2015, 2015.

Lauritzen, P. H., Nair, R. D., Herrington, A. R., Callaghan, P., Goldhaber, S., Dennis, J. M., Bacmeister, J. T., Eaton, B. E., Zarzycki, C. M., Taylor, M. A., and et al.: NCAR release of Cam-SE in Cesm2.0: A reformulation of the spectral element dynamical core in dry-mass vertical coordinates with comprehensive treatment of condensates and Energy, Journal of Advances in Modeling Earth Systems, 10, 1537–1570, https://doi.org/10.1029/2017ms001257, 2018.

Lavers, D. A., Ralph, F. M., Waliser, D. E., Gershunov, A., and Dettinger, M. D.: Climate change intensification of horizontal water vapor transport in CMIP5, Geophysical Research Letters, 42, 5617–5625, https://doi.org/10.1002/2015gl064672, 2015.

Lawrence, D. M., Fisher, R. A., Koven, C. D., Oleson, K. W., Swenson, S. C., Bonan, G., Collier, N., Ghimire, B., van Kampenhout, L., Kennedy, D., et al.: The Community Land Model version 5: Description of new features, benchmarking, and impact of forcing uncertainty, Journal of Advances in Modeling Earth Systems, 11, 4245–4287, 2019.

Lipscomb, W. H., Price, S. F., Hoffman, M. J., Leguy, G. R., Bennett, A. R., Bradley, S. L., Evans, K. J., Fyke, J. G., Kennedy, J. H., Perego, M., Ranken, D. M., Sacks, W. J., Salinger, A. G., Vargo, L. J., and Worley, P. H.: Description and evaluation of the Community Ice Sheet Model (CISM) v2.1, Geoscientific Model Development, 12, 387–424, https://doi.org/https://doi.org/10.5194/gmd-12-387-2019, 2019.

Mattingly, K. S., Mote, T. L., and Fettweis, X.: Atmospheric River impacts on Greenland Ice Sheet Surface Mass Balance, Journal of Geophysical Research: Atmospheres, 123, 8538–8560, https://doi.org/10.1029/2018jd028714, 2018.

Mattingly, K. S., Mote, T. L., Fettweis, X., van As, D., Van Tricht, K., Lhermitte, S., Pettersen, C., and Fausto, R. S.: Strong summer atmospheric rivers trigger greenland ice sheet melt through spatially varying surface energy balance and cloud regimes, Journal of Climate, 33, 6809–6832, https://doi.org/10.1175/jcli-d-19-0835.1, 2020.

Mattingly, K. S., Turton, J. V., Wille, J. D., Noel, B., Fettweis, X., Rennermalm, A. K., and Mote, T. L.: Increasing extreme melt in northeast Greenland linked Foehn winds and Atmospheric Rivers, Nature Communications, 14, https://doi.org/10.1038/s41467-023-37434-8, 2023.

McClenny, E. E., Ullrich, P. A., and Grotjahn, R.: Sensitivity of atmospheric river vapor transport and precipitation to uniform sea surface temperature increases, Journal of Geophysical Research: Atmospheres, 125, https://doi.org/10.1029/2020jd033421, 2020.

Neff, W., Compo, G. P., Ralph, F. M., and Shupe, M. P.: Continental heat anomalies and the extreme melting of the Greenland ice surface in 2012 and 1889, Journal of Geophysical Research: Atmospheres, 119, 6520–6536, https://doi.org/10.1002/2014JD021470, 2014.

Noël, B., van de Berg, W. J., Van Wessem, J. M., Van Meijgaard, E., Van As, D., Lenaerts, J., Lhermitte, S., Kuipers Munneke, P., Smeets, C., Van Ulft, L. H., et al.: Modelling the climate and surface mass balance of polar ice sheets using RACMO2–Part 1: Greenland (1958–2016), The Cryosphere, 12, 811–831, 2018.

Patricola, C., O'Brien, J., Risser, M., Rhoades, A., O'Brien, T., Ullrich, P., Stone, D., and Collins, W.: aximizing ENSO as a source of western US hydroclimate predictability, 54, 351–372, https://doi.org/10.1007/s00382-019-05004-8, 2020.

Payne, A. E., Demory, M. E., Leung, L. R., Ramos, A. M., Shields, C. A., Rutz, J. L., Siler, N., Villarini, G., Hall, A., and Ralph, F. M.: Responses and impacts of atmospheric rivers to climate change, Nature Reviews Earth and Environment, 1, 143–157, https://doi.org/10.1038/s43017-020-0030-5, 2020.

Pollard, D. and Groups, P. P.: Comparisons of ice-sheet surface mass budgets from Paleoclimate Modeling Intercomparison Project (PMIP) simulations, Global and Planetary Change, 24, 79–106, 2000.

Rhoades, A. M., Jones, A. D., O'Brien, T. A., O'Brien, J. P., Ullrich, P. A., and Zarzycki, C. M.: Influences of North Pacific Ocean domain extent on the western U.S. winter hydroclimatology in variable-Resolution CESM, Journal of Geophysical Research: Atmospheres, 125, https://doi.org/10.1029/2019jd031977, 2020a.

Rhoades, A. M., Jones, A. D., Srivastava, A., Huang, H., O'Brien, T. A., Patricola, C. M., Ullrich, P. A., Wehner, M., and Zhou, Y.: The Shifting Scales of western U.S. landfalling atmospheric rivers under climate change, Geophysical Research Letters, 47, https://doi.org/10.1029/2020gl089096, 2020b.

Rutz, J. J., Shields, C. A., Lora, J. M., Payne, A. E., Guan, B., Ullrich, P., O'Brien, T., Leung, L. R., Ralph, F. M., Wehner, M., and et al.: The Atmospheric River Tracking Method Intercomparison Project (ARTMIP): Quantifying uncertainties in Atmospheric River Climatology, Journal of Geophysical Research: Atmospheres, 124, 13 777–13 802, https://doi.org/10.1029/2019jd030936, 2019.

Shields, C. A., Rutz, J. J., Leung, L.-Y., Ralph, F. M., Wehner, M., Kawzenuk, B., Lora, J. M., McClenny, E., Osborne, T., Payne, A. E., and et al.: Atmospheric River Tracking Method Intercomparison Project (ARTMIP): Project Goals and Experimental Design, Geoscientific Model Development, 11, 2455–2474, https://doi.org/10.5194/gmd-11-2455-2018, 2018.

Shields, C. A., Wille, J. D., Marquardt Collow, A. B., Maclennan, M., and Gorodetskaya, I. V.: Evaluating uncertainty and modes of variability for Antarctic Atmospheric Rivers, Geophysical Research Letters, 49, https://doi.org/10.1029/2022gl099577, 2022.

Team, E. J. S., Balaji, V., Boville, B., Collins, N., Craig, T., Cruz, C., da Silva, A., DeLuca, C., Eaton, B., Hallberg, B., et al.: ESMF User Guide, Tech. rep., 2021.

Ullrich, P. A. and Taylor, M. A.: Arbitrary-Order Conservative and Consistent Remapping and a Theory of Linear Maps: Part I, Mon. Wea. Rev., 143, 2419–2440, https://doi.org/10.1175/MWR-D-14-00343.1, 2015.

Ullrich, P. A., Zarzycki, C. M., McClenny, E. E., Pinheiro, M. C., Stansfield, A. M., and Reed, K. A.: TempestExtremes v2. 1: a community framework for feature detection, tracking and analysis in large datasets, Geoscientific Model Development Discussions, pp. 1–37, 2021.

van Kampenhout, L., Lenaerts, J. T., Lipscomb, W. H., Lhermitte, S., Noël, B., Vizcaíno, M., Sacks, W. J., and van den Broeke, M. R.: Present-day Greenland Ice Sheet climate and surface mass balance in CESM2, Journal of Geophysical Research: Earth Surface, 125, 2020.

Viceto, C., Gorodetskaya, I. V., Rinke, A., Maturilli, M., Rocha, A., and Crewell, S.: Atmospheric rivers and associated precipitation patterns during the ACLOUD and PASCAL campaigns near Svalbard (May–June 2017): case studies using observations, reanalyses, and a regional climate model, Atmospheric Chemistry and Physics, 22, 441–463, https://doi.org/10.5194/acp-22-441-2022, 2022.

Zarzycki, C. M. and Jablonowski, C.: Experimental tropical cyclone forecasts using a variable-resolution global model, Monthly Weather Review, 143, 4012–4037, https://doi.org/10.1175/mwr-d-15-0159.1, 2015.

Zarzycki, C. M., Jablonowski, C., Thatcher, D. R., and Taylor, M. A.: Effects of localized grid refinement on the general circulation and climatology in the community atmosphere model, Journal of Climate, 28, 2777–2803, https://doi.org/10.1175/jcli-d-14-00599.1, 2015.

Zhang, P., Chen, G., Ma, W., Ming, Y., and Wu, Z.: Robust Atmospheric River response to global warming in idealized and comprehensive climate models, Journal of Climate, p. 1–52, https://doi.org/10.1175/jcli-d-20-1005.1, 2021.

Zhang, P., Chen, G., Ting, M., Ruby Leung, L., Guan, B., and Li, L.: More frequent atmospheric rivers slow the seasonal recovery of Arctic Sea Ice, Nature Climate Change, 13, 266–273, https://doi.org/10.1038/s41558-023-01599-3, 2023.

Zhou, Y., O'Brien, T. A., Collins, W. D., Shields, C. A., Loring, B., and Elbashandy, A. A.: Characteristics and variability of winter northern Pacific Atmospheric River Flavors, Journal of Geophysical Research: Atmospheres, 127, https://doi.org/10.1029/2022jd037105, 2022.